Peregrine Falcon: Design and Experimentation of a Folding and Launchable Quadcopter Drone

Guangxin Wu [1,2], Xinbiao Pei [1,3], Dong Wang [4], Lijun Nan [4], Dong Wang [1,2], Hejia Zhou [4] and Yue Bai [1,2,*]

1   Changchun Institute of Optics, Fine Mechanics and Physics, Chinese Academy of Sciences, Changchun 130033, China; wuguangxin20@mails.ucas.ac.cn (G.W.); peixinbiao@ciomp.ac.cn (X.P.); wangdong21b@mails.ucas.ac.cn (D.W.)
2   University of Chinese Academy of Sciences, Beijing 100049, China
3   Changchun Changguang Boxiang UAV Co., Ltd., Changchun 130033, China
4   China North Vehicle Research Institute, Beijing 100072, China; wangdong173@mails.ucas.ac.cn (D.W.); nanlijun@126.com (L.N.); zhouhejia277@gmail.com (H.Z.)
*   Correspondence: baiy@ciomp.ac.cn

Abstract: This article describes a quadcopter drone with foldable arms, which we have named the Peregrine Falcon. It can take off from a moving vehicle by barrel launching and perform its mission in the air after autonomously spreading its arms. The design helps the drone to be put into operation quickly, which is a great advantage for applications in industries such as forest fire reconnaissance. This paper introduces the design process of the Peregrine Falcon from the aspects of structure, avionics and control algorithm, and proposes control compensation methods for the large attitude change generated during the barrel launching process and the vertical drift problem after impact, respectively. The stability and feasibility of the Peregrine Falcon in the static and dynamic launching process are verified by flying experiments.

Keywords: quadcopter drone; arm foldable mechanism; barrel launching; dynamic modeling; controller design; outdoor flight

1. Introduction

In recent years, drones have found widespread application in both civil and military domains. Among them, multi-rotor drones have gained popularity due to their superior flexibility and ease of operation compared to fixed-wing drones [1]. They can take off and land in confined spaces, which makes them ideal for urban inspections, anti-terrorism reconnaissance, and forest firefighting [2–4]. However, the rotating blades pose risks to nearby personnel, especially during automatic, unsupervised operations. Additionally, many multi-rotor drones have lengthy deployment times, are not easily operable from moving vehicles, and occupy significant space. Therefore, in crowded and dynamic environments, there is a critical need for a precise and rapid automated takeoff method to ensure safe operations away from personnel.
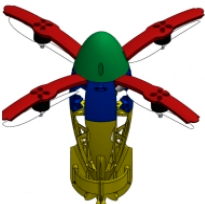
In response to these challenges, various drones with innovative arm-folding designs have been developed [5–7]. Jiulong Xu created an arm-folding drone [8] that requires users to manually unfold the arms, significantly slowing down maneuverability and posing a risk of premature activation of the paddles. Researchers at Shanghai Jiao Tong University designed the Nezha-F, a hybrid aerial–underwater vehicle featuring a foldable and self-deployable arm mechanism driven by a piston variable buoyancy system (PVBS). This design aims to minimize excessive underwater drag caused by aerial structures [9]. Similarly, the Nezha-III, developed by the same team, employs a folding mechanism that retracts its six motor arms underwater to reduce hydrodynamic drag. The vehicle weighs 18 kg, and its folding mechanism, which takes 11 to 13 s to deploy, weighs 280 g [10]. Additionally, Yang Liu et al. at Zhejiang University applied the principles of bird wing

retraction to design a foldable amphibious unmanned aerial vehicle (UAV) capable of expanding and contracting its wings [11].

To minimize time loss in critical areas, some drones utilize a throw launch method [12,13], while others can autonomously transition from a simple ballistic launch to flight, enabling them to quickly reach mission altitude [14–18]. In contrast, drones launched via barrel shots experience greater instantaneous acceleration. However, the higher exit velocity allows for a longer retention time in the air, providing more time for attitude stabilization. Additionally, the French–German Research Institute of Saint Louis (ISL) has proposed a gun-launched micro air vehicle (GLMAV), although the article does not validate the transition from projectile flight to MAV flight [19,20]. The California Institute of Technology has developed ballistic-launched prototypes, including a four-rotor [21] and a six-rotor [22] drone called SQUID. The former validates the stability of static and dynamic catapult UAVs but employs a spreading arm mechanism that requires manual control. The latter demonstrates an autonomous transition from passive to vision-based active stabilization, though it lacks validation from mobile launch test experiments.

This paper proposes a deformable drone with folding arms that can be launched by ballistic launch and named the Peregrine Falcon. When the Peregrine Falcon is in the launch barrel, its arms are in a folded state, and the Peregrine Falcon carries out an autonomous spreading of its arms when it is launched into the air. Table 1 lists the parameters and characteristics of the Peregrine Falcon and other UAVs of the same type. Compared to other UAVs of the same type, the Peregrine Falcon's arms can be folded repeatedly without the need for removal or replacement. The folding mechanism is controlled by a pulse width modulation (PWM) signal from the flight controller to the servo for spreading the arms, making it easier to use. In addition, the Peregrine Falcon with its payload can be launched on the move. Figure 1 below shows the working mode of the Peregrine Falcon. The Peregrine Falcon performs its mission autonomously after launching through the launch barrel. For UAV control strategies, PID control has been the natural choice for stabilizing quadcopter UAVs due to its simplicity and robustness [23]. For the Peregrine Falcon, the impact will produce large attitude changes [24] and the vertical direction of the drift problem, respectively, and we proposed a control compensation method and performed a physical experiment to verify its effect.

Table 1. Parameters and characteristics of the Peregrine Falcon and similar drones.

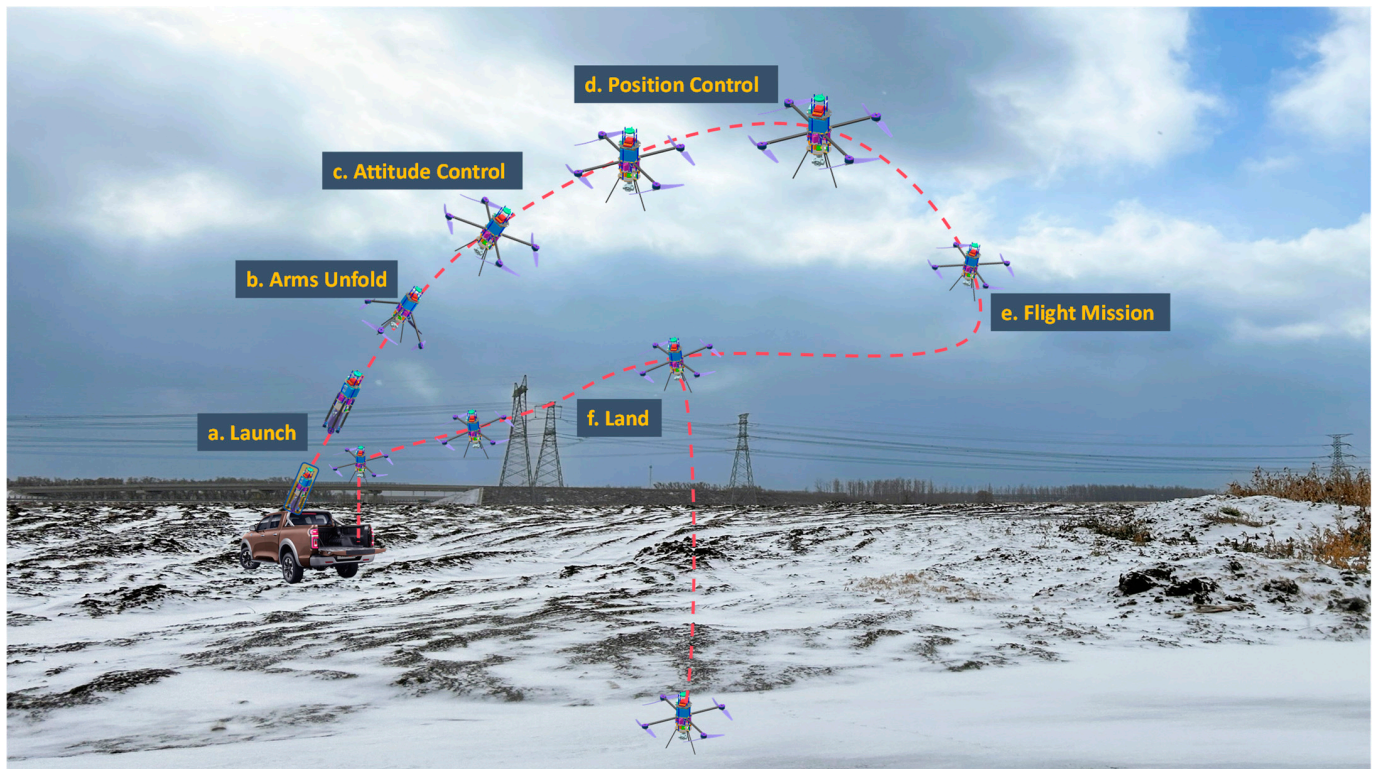| Aircraft Model	Picture	Weight	Folded Diameter	Support Mobile Deployment	Support Autonomous Arms
Four-rotor SQUID		0.53 kg	83 mm	Yes	No
Six-rotor SQUID		3.3 kg	150 mm	No	Yes
Peregrine Falcon		2.56 kg	120 mm	Yes	Yes

Figure 1. Schematic diagram of the working mode.

The remainder of this paper is structured as follows: Section 2 focuses on the mechanical design of the drone, including power matching, the impact resistance design, and control unit; Section 3 performs dynamic and kinematic modeling for the Peregrine Falcon's four-rotor structure; Section 4 introduces the software control algorithm; Section 5 performs simulation and flying experimental validation; and Sections 6 and 7 provide a summary and prospects for future work, respectively.

2. Mechanical Design

This part mainly focuses on the design index of the Peregrine Falcon for power matching, the fuselage is analyzed for impact resistance, and the composition of the whole airframe is shown in Figure 2.
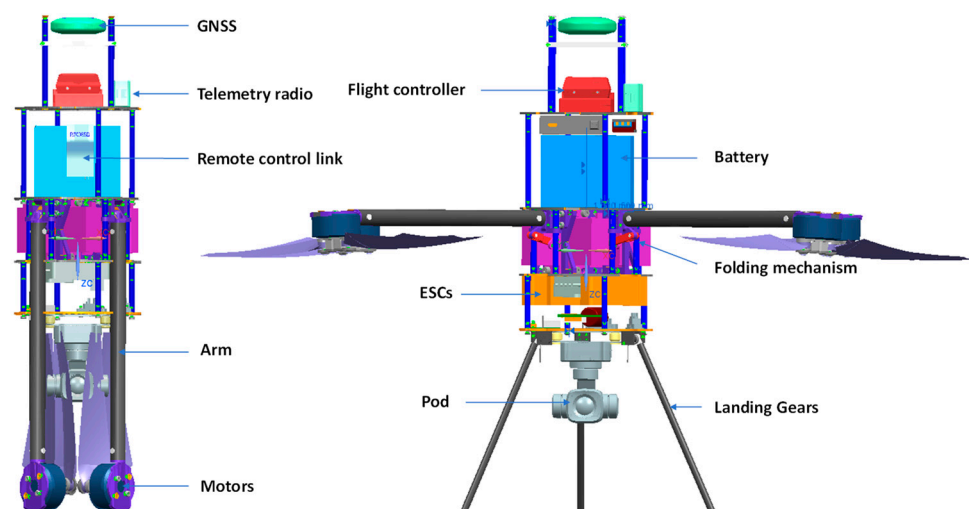

Figure 2. Physical assembly drawing and detailed display. Also, GNSS: global navigation satellite system, ESCs: electronic speed controllers.

2.1. Applicable Requirements

Considering the application scenes of the rapid deployment of the barrel-launching method, it is necessary to specify the maximum take-off weight, flight time, instantaneous impact that can be withstood, and other indexes of the drone. For comprehensively different needs, the parameter specifications of the Peregrine Falcon are now designed, as shown in Table 2.

Table 2. Design specifications.

Design Parameter	Value
Maximum takeoff weight	$\geq$2.5 kg
Flight endurance	$\geq$10 min
Maximum speed	$\geq$10 m/s
Withstand maximum momentary impact	$\leq$75 G [1]

[1] Where the value of G represents a multiple of the acceleration of gravity, take 1 G = 9.8 m/s^2.

2.2. Driving Unit Match

The power is selected according to the maximum takeoff weight. The propeller size, efficiency and aerodynamic performance are the key features that determine the size and overall weight of the drone. Based on the principle of minimum volume, the carbon fiber composite folding propeller with a small volume and high efficiency ratio is selected as the power component of the drone. The selected paddle size is 12 inches with a pitch of 5 inches, weighing 17.5 g, and the thrust–speed data from the paddle supplier, Zhongshan Sunny-Sky Model Co., Ltd., Zhuhai, China, are shown in Figure 3. Thrust increases gradually as the paddle rotates faster.
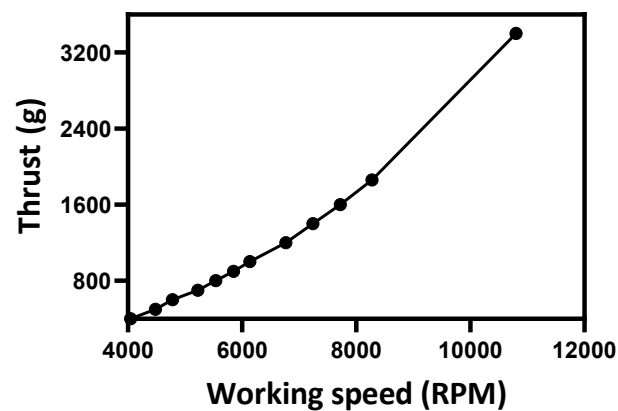

Figure 3. Thrust–speed curve.

The maximum rotational speed of the single propeller is 10,800 rpm, which corresponds to 3.4 kg of thrust. A total of 50% of the rotational speed of the single propeller is 5400 rpm, which corresponds to 0.8 kg of thrust. The theoretical maximum thrust that the drone can generate is calculated to be

$$F_{max} = 3.4 \text{ kg} \times 4 = 13.6 \text{ kg} \tag{1}$$

The thrust at 5400 rpm for the drone was as follows:

$$F_{mid} = 0.8 \text{ kg} \times 4 = 3.2 \text{ kg} \tag{2}$$

In order to reserve a certain control margin, the thrust F_{mid_loss} at 5400 rpm is calculated by applying a 20% loss of aerodynamic efficiency as follows:

$$F_{mid\_loss} = 0.8 \times F_{mid} = 2.56 \text{ kg} \tag{3}$$

From this calculation, the total thrust of the drone obtained is greater than 2.5 kg, which meets the design requirements.

2.3. Energy Match

According to the design of the drone weighing 2.56 kg and matched according to the thrust–current data in Table 3, the theoretical total current is calculated as follows:

$$I = 3.7 \times 4 = 14.8\text{A} \tag{4}$$

Table 3. The thrust–current data from the motor supplier, Zhongshan Sunny-Sky Model Co., Ltd., China.

Items	Value 1	Value 2	Value 3	Value 4	Value 5	Value 6	Value 7	Value 8	Value 9	Value 10	Value 11
Thrust (g)	200	300	400	500	600	700	800	900	1000	1200	1395
Current (A)	0.5	0.9	1.4	1.9	2.4	3	3.7	4.4	5.1	6.7	8.5

Choose a small volume 6 s battery capacity of 1550 mAh, weighing 251 g. Use two parallel batteries with a total capacity C_b of 3100 mAh, and a total weight of the battery of 502 g. According to the calculation of the remaining 15% of the battery capacity, the minimum remaining capacity is as follows:

$$C_{min} = 15\% \times C_b \tag{5}$$

From Equations (4) and (5), the theoretical flight time is calculated as follows:

$$T_{nom} = (C_b - C_{min})/1000 \times 60/I = 10.68 \text{ min} \tag{6}$$

2.4. Folding Mechanism

As shown in Figure 4, the design of the controllable auto-folding mechanism uses four independent servo linkage mechanisms. The flight control system regulates the PWM output of the servos to realize the control of arm closing and unfolding in a controlled time, and it can be reused. Keeping the PWM at a high output level when the Peregrine Falcon is powered on can realize the self-locking function, and keeping the PWM at a low input level can flatten the arms.
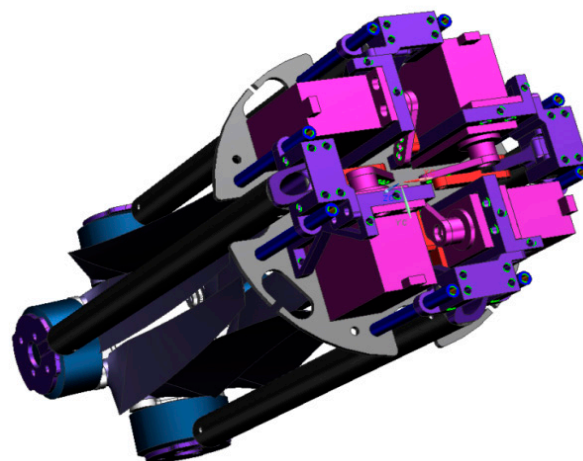

Figure 4. Folding mechanism.

2.5. Impact of the Barrel Launch Analysis

The Peregrine Falcon body is supported by carbon fiber plates and copper pillars, and the motor base and arm folding area are made of hard aluminum alloy. The arm is constructed with carbon fiber tubes. Since the instantaneous impact acceleration of the barrel launch is between 50–75 G, a static analysis must be conducted for the designed drone.

The thrust *F* is applied to the motor ends of the four arms as follows:

$$F = Mga_{max} \tag{7}$$

where *M* is the mass of the whole machine, 2.56 kg, *g* is the gravitational constant, and a_{max} is the maximum instantaneous impact acceleration.

Set the part connected to the outer shell as a fixed constraint and calculate the displacements and stresses generated by the structure. After finite element calculation, the maximum displacement is the top of the arm, as shown in Figure 5, the deformation is 1.5 mm, and the maximum stress is generated at the connection between the arm and the carbon fiber plate with a stress value of 382.58 MPa. Although it is much smaller than the yield strength of the carbon fiber material, it is close to that of the rigid aluminum alloy material, and the acceleration impact of 75 G in a short period of time does not exceed the yield strength, which meets the yield limit design requirements.
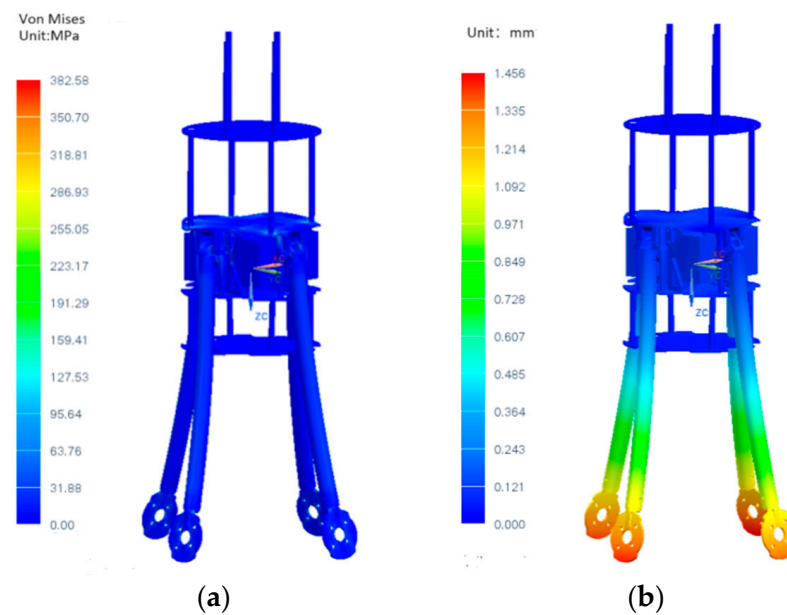

Figure 5. Stress and displacement: (**a**) stress (**b**) displacement.

2.6. Flight Control Units

The hardware core processor of the controller is selected from the STM32H7 series, equipped with triple-redundant inertial measurement units (IMUs), including ICM42688-P, BMI088, and ICM20649, as well as an RM3100 compass and MS5611 barometer. Regarding servo precautions, the servo signal lines are often close to the motor power lines, and servo cables or shielded cables with strong anti-jamming capabilities must be selected. The electrical system connections are shown in Figure 6.
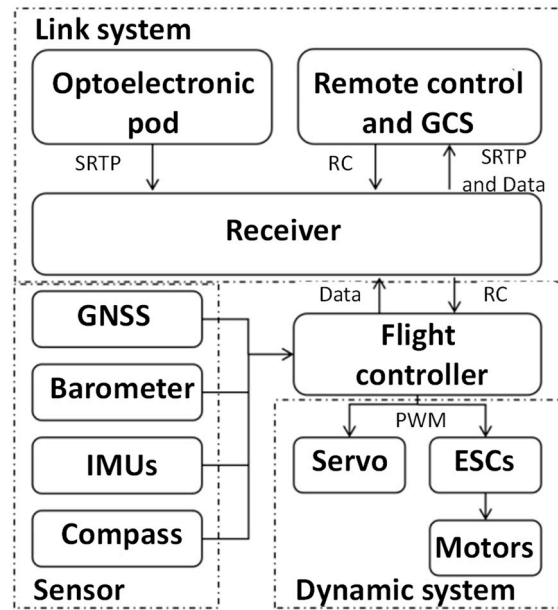
Figure 6. Electrical system connection diagram. Also, GCS: ground control system, SRTR: real-time transport protocol, RC: remote control, IMUs: inertial measurement units.

3. Dynamic Modeling

In this part, we will model the kinematics and dynamics of the Peregrine Falcon. Considering that the Euler angles have the defect of a universal lock [25], the quaternion method is used for modeling in order to avoid ambiguity.

As shown in Figure 7, the drone adopts a four-rotor structure. It contains two coordinate systems, the inertial coordinate system $O^e\{x^e, y^e, z^e\}$, and body coordinate system $O^b\{x^b, y^b, z^b\}$. The attitude of the drone is represented by the unit quaternion $q = \begin{bmatrix} q_0 & q_1 & q_2 & q_3 \end{bmatrix}^T \in \mathcal{R}^4$, and it satisfies the constraint $q_0^2 + q_1^2 + q_2^2 + q_3^2 = 1$. Its kinematic model is as follows:

$$\begin{cases} \dot{\boldsymbol{p}}^e = \boldsymbol{v}^e \\ \dot{q}_0 = -\frac{1}{2}\boldsymbol{q}_v^T \cdot \omega^b \\ \dot{\boldsymbol{q}}_v = \frac{1}{2}(q_0 I_3 + [\boldsymbol{q}_v]_x)\omega^b \end{cases} \tag{8}$$
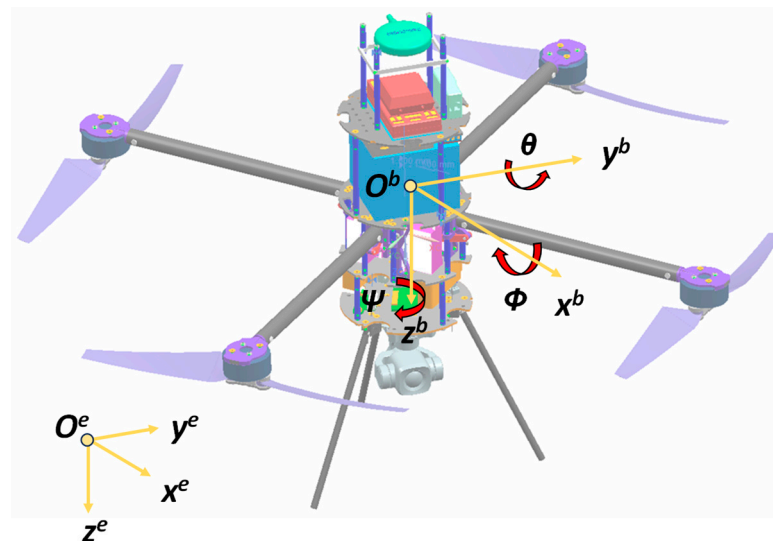

Figure 7. Coordinate system of the Peregrine Falcon.

Its dynamics are modeled as follows:

$$\begin{cases} \dot{v}^b = -\left[\omega^b\right] \times v^b + F^b/m \\ J\cdot\dot{\omega}^b = -\omega^b \times \left(J\cdot\omega^b\right) + M^b \end{cases} \tag{9}$$

where $p^e \in \mathcal{R}^3$ and $v^e \in \mathcal{R}^3$ denote the position vector and velocity vector of the drone in the inertial coordinate system, and vector $q_v = \begin{bmatrix} q_1 & q_2 & q_3 \end{bmatrix}^T \in \mathcal{R}^3$, ω^b denotes the angular velocity of the body. $I_3 \in \mathcal{R}^{3\times3}$ is a unit matrix, and $J = diag\begin{pmatrix} J_x & J_y & J_z \end{pmatrix} \in \mathcal{R}^{3\times3}$ denotes the aircraft's moment of inertia. m denotes the mass of the aircraft, and F^b and M^b denote the total thrust and the total moment, respectively, for any vector $a = \begin{bmatrix} a_x & a_y & a_z \end{bmatrix}^T \in \mathcal{R}^3$. The symbol $[a]_x$ is defined as follows:

$$[a]_x = \begin{bmatrix} 0 & -a_z & a_y \\ a_z & 0 & -a_x \\ -a_y & a_x & 0 \end{bmatrix} \tag{10}$$

The rotation matrix that transforms the Peregrine Falcon from the body coordinate system to the inertial coordinate system is expressed in quaternions as follows:

$$R_e^b = \begin{bmatrix} p_{11} & p_{12} & p_{13} \\ p_{21} & p_{22} & p_{23} \\ p_{31} & p_{32} & p_{33} \end{bmatrix} \tag{11}$$

where $p_{11} = q_0^2 + q_1^2 - q_2^2 - q_3^2$, $p_{12} = 2(q_1q_2 - q_0q_3)$, $p_{13} = 2(q_1q_3 + q_0q_2)$, $p_{21} = 2(q_1q_2 + q_0q_3)$, $p_{22} = q_0^2 - q_1^2 + q_2^2 - q_3^2$, $p_{23} = 2(q_2q_3 - q_0q_1)$, $p_{31} = 2(q_1q_3 - q_0q_2)$, and $p_{32} = 2(q_2q_3 + q_0q_1)$, $p_{33} = q_0^2 - q_1^2 - q_2^2 + q_3^2$.

4. Control Algorithm Design

The whole process of launching includes the following phases: the cylinder standby phase, the launch phase, the arm spreading phase, the attitude stabilization phase, the climb rate control phase, and the position stabilization phase. First, the drone turns on the power in the standby phase inside the barrel and enters the launch phase when it receives the launch command, at which time the drone unlocks. Then, when the drone comes out of the barrel and enters the arm spreading phase, the drone starts to spread its arms autonomously. After arm spreading is completed, the drone enters the attitude stabilization phase, and the drone starts to stabilize its attitude. It is not until the attitude is stabilized to a certain extent that the climb rate of the drone starts to be controlled. Finally, in the position stabilization phase, the drone starts to perform position control.

This part mainly focuses on the two main processes of stabilization control under large attitude change after barrel shooting and the rapid stabilization control algorithm for the climb rate after impact.

4.1. Attitude Control Algorithm Design

Since the Peregrine Falcon is launched at an angle of 70 degrees, it will produce large attitude changes after being launched into the air. Therefore, an attitude control algorithm needs to be designed to solve its stabilization and fast convergence during large attitude changes in the air.

To ensure that the Peregrine Falcon has a better attitude tracking speed, this paper designs a feedforward control algorithm for this type of model. As Figure 8 shows the block diagram of the control algorithm designed; considering that the attitude feedforward is limited by the maximum angular acceleration, the square root controller control is added to the feedforward control.
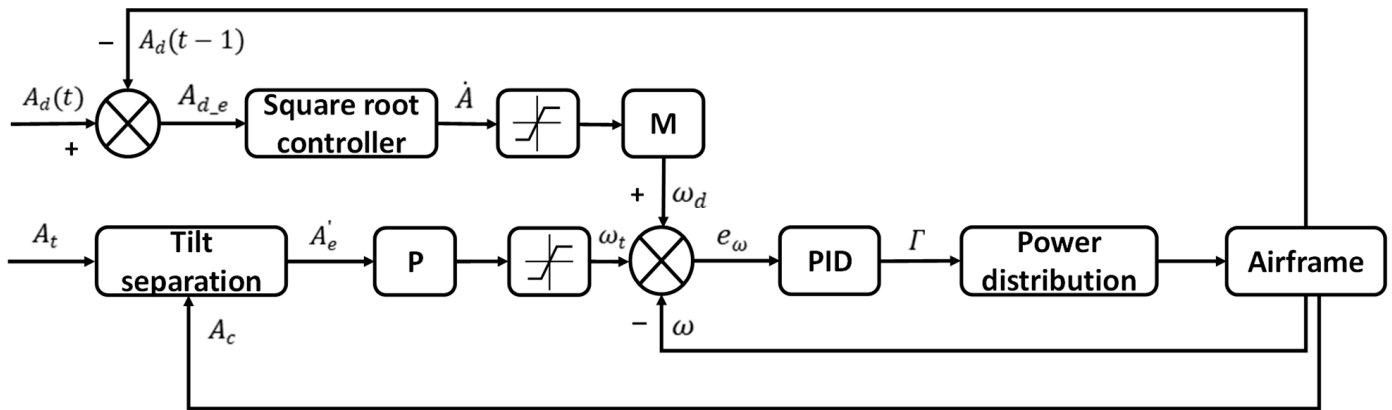
Figure 8. Attitude controller structure.

First, calculate the desired angular error as follows:

$$A_{d\_e} = A_d(t) - A_d(t-1) \tag{12}$$

Then, the expected Eulerian angular velocity $\dot{A}$ satisfies the following equation:

$$\dot{A} = \begin{cases} \sqrt{2 * a_{max} * \left(A_{d\_e} - \frac{a_{max}}{2*k^2}\right)} & A_{d\_e} \geq a_{max}/k^2 \\ -\sqrt{2 * a_{max} * \left(-A_{d\_e} - \frac{a_{max}}{2*k^2}\right)} & A_{d\_e} \leq -a_{max}/k^2 \\ k * A_{d\_e} & -a_{max}/k^2 < A_{d\_e} < a_{max}/k^2 \end{cases} \tag{13}$$

where k is a constant, a_{max} is the maximum angular acceleration, and $A_d(t)$ and $A_d(t-1)$ are the desired attitude angles at this and the previous moment, respectively.

Convert the desired Eulerian angular velocity to body angular velocity as follows:

$$\omega_d = M\dot{A} \tag{14}$$

The transformation matrix M is as follows:

$$M = \begin{bmatrix} 1 & 0 & -sin\phi \\ 0 & cos\phi & cos\theta sin\phi \\ 0 & -sin\phi & cos\theta cos\phi \end{bmatrix} \tag{15}$$

Since the control process needs to be stabilized first for the horizontal plane attitude [26], the axial angle separation method is used to stabilize the roll angle and pitch angle first during the control process to obtain the desired attitude and the current attitude error. Combined with Equation (11), the current attitude quaternion $A_c = q$ is obtained by transforming the current attitude rotation matrix, where

$$\begin{cases} q_0 = sign(q_0) * 0.5 * \sqrt{1 + p_{11} + p_{22} + p_{33}} \\ q_1 = sign(q_0) * (p_{32} - p_{23}) * 0.5 * \sqrt{1 + p_{11} - p_{22} - p_{33}} \\ q_2 = sign(q_0) * (p_{13} - p_{31}) * 0.5 * \sqrt{1 - p_{11} + p_{22} - p_{33}} \\ q_3 = sign(q_0) * (p_{21} - p_{12}) * 0.5 * \sqrt{1 - p_{11} - p_{22} + p_{33}} \end{cases} \tag{16}$$

The initial target attitude quaternion is $A_t = [q_{t0} \ q_{t1} \ q_{t2} \ q_{t3}]^T$. The unit vectors e_{zt}^B and e_z^B of the desired and current quaternions in the Z-axis of the body coordinate system are obtained.

$$e_z^B = \begin{bmatrix} 2(q_0 q_2 + q_1 q_3) \\ 2(q_2 q_3 - q_0 q_1) \\ 2(q_0^2 - q_1^2 - q_2^2 + q_3^2) \end{bmatrix}$$
$$e_{zt}^B = \begin{bmatrix} 2(q_{t0} q_{t2} + q_{t1} q_{t3}) \\ 2(q_{t2} q_{t3} - q_{t0} q_{t1}) \\ 2(q_{t0}^2 - q_{t1}^2 - q_{t2}^2 + q_{t3}^2) \end{bmatrix} \tag{17}$$

The axis angle and tilt error quaternion are calculated from Equation (17) as follows:

$$\alpha = arccos\left(e_z^B, \ e_{zt}^B\right)$$
$$A_e = \begin{bmatrix} cos(\alpha/2) \\ sin(\alpha/2) \frac{e_z^B \times e_{zt}^B}{\|e_z^B \times e_{zt}^B\|} \end{bmatrix} \tag{18}$$

The tilt error quaternion is transferred to the inertial coordinate system as follows:

$$A_e^B = A_c^{-1} \cdot A_e \cdot A_c \tag{19}$$

The tilted expectation quaternion A_{t_tilt} is obtained from Equation (19) as follows:

$$A_{t\_tilt} = A_c \cdot A_e^B \tag{20}$$

The rotational expectation quaternion A_{t_rot} is obtained from Equation (20) as follows:

$$A_{t\_rot} = A_{t\_tilt}^{-1} \cdot A_t \tag{21}$$

Recompose the expectation quaternion A_t' after restricting it with respect to the rotation quaternion

$$A_t' = A_{t\_tilt} \cdot A_{t\_rot} \tag{22}$$

The new expected error quaternion is as follows:

$$A_e' = A_c^{-1} \cdot A_t' \tag{23}$$

Disregarding the first term of A_e', after the P-controller we can obtain the following formula:

$$\omega_t = K_P * A_e' \tag{24}$$

where K_P is the outer loop constant variable, and the angular velocity error is calculated from Equations (14) and (24).

$$e_\omega = \omega_t + \omega_d - \omega \tag{25}$$

where is the current angular velocity of ω, and then as an inner loop expectation for angular velocity loop design

$$\Gamma = K_p * e_\omega + K_i * \int e_\omega dt + K_d * \dot{e}_\omega \tag{26}$$

where K_p, K_i, and K_d are constant variables and Γ is the angular velocity loop system output, respectively.

4.2. Climb Rate Control Algorithm Design

Since the Peregrine Falcon is subjected to a vertical upward kinetic energy component during barrel launching and the Peregrine Falcon itself requires a large throttle input to complete the attitude correction, the use of the conventional cascaded PID to control the altitude will result in a slow convergence. To address this problem, this paper proposes to prioritize the control of the climb rate of the Peregrine Falcon and combines feedforward control to quickly complete the tracking of the target climb rate.

Wind drag and heat losses to the total energy, as well as the energy generated by aircraft power, are neglected to yield

$$E_{total} = mgh_c + \frac{1}{2}mv_{zt}^2 \tag{27}$$

where denotes E_{total} the total energy of the aircraft, m is the mass of the aircraft, g is the gravitational acceleration constant, h_c is the current aircraft altitude, and v_{zt} is the target rate of climb at the current altitude of the aircraft.

The energy changes within the Peregrine Falcon can be thought of as follows:

$$mg\Delta h_{max} = \frac{1}{2}mv_{zmax}^2 \tag{28}$$

where v_{zmax} is the maximum rate of climb of the Peregrine Falcon transformed by the impact energy, and the height of change is $\Delta h_{max} = h_{max} - h_0$. h_{max} is the maximum height of the Peregrine Falcon transformed by the impact energy. $h_0 = (E_{total} - \frac{1}{2}mv_{zmax}^2)/mg$ is the starting height.

From Equations (27) and (28), the target rate of climb at the current altitude is

$$v_{zt} = \sqrt{v_{zmax}^2 - 2g(h_c - h_0)} \tag{29}$$

The climb target acceleration is calculated using the P-controller as follows:

$$a_{zt} = (v_{zt} + v_{zf} - v_{zc}) * k_v \tag{30}$$

where k_v is a constant. The acceleration error is calculated as follows:

$$e_{az} = a_{zt} + a_{zf} - a_{zc} \tag{31}$$

The throttle output is

$$t_z = e_{az} * k_p + \int e_{az}dt * k_i + \dot{e}_{az} * k_d \tag{32}$$

where k_p, k_i, and k_d are constants, respectively, and v_{zf} and a_{zf} are velocity feedforward and acceleration feedforward, respectively. v_{zc} and a_{zc} are the actual velocity and acceleration, respectively. The block diagram of the algorithm structure is shown in Figure 9.
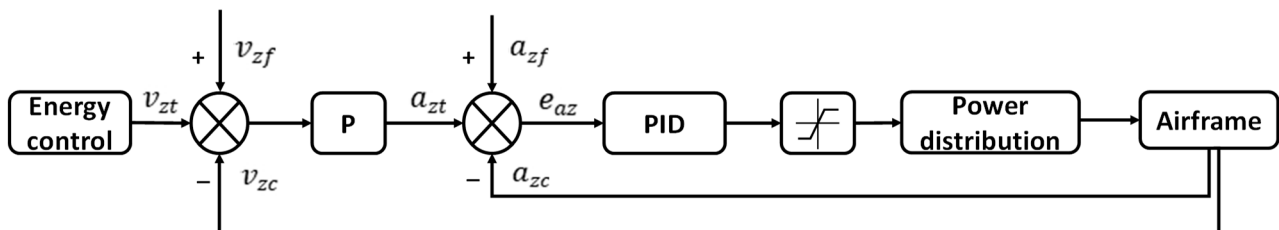

Figure 9. Climb rate controller structure.

5. Simulation and Flying Experiments

This section describes three experiments: a simulated load experiment, a static barrel launch experiment, and a dynamic barrel launch experiment. During the experiments, the data of the drone are recorded by the flight controller, including the attitude, altitude, position, speed, voltage, and other information. Images were taken by a mobile phone, a ground camera, and a DJI mini2 drone.

5.1. Simulated Load Experiment

We set up a simulated load with the same mass as the Peregrine Falcon drone, as shown in Figure 10a. It carries an accelerometer with a maximum range of 200 G and records acceleration data at a frequency of 1000 hz. The maximum acceleration generated by the impact of the launch tube at the moment of launching at a 70-degree swing is measured to be 72.65 G, as shown in Figure 10b. The design meets the requirement of less than 75 G maximum acceleration and can effectively test whether the body of the drone can withstand the instantaneous impact of the maximum acceleration close to 75 G in the launch tube.
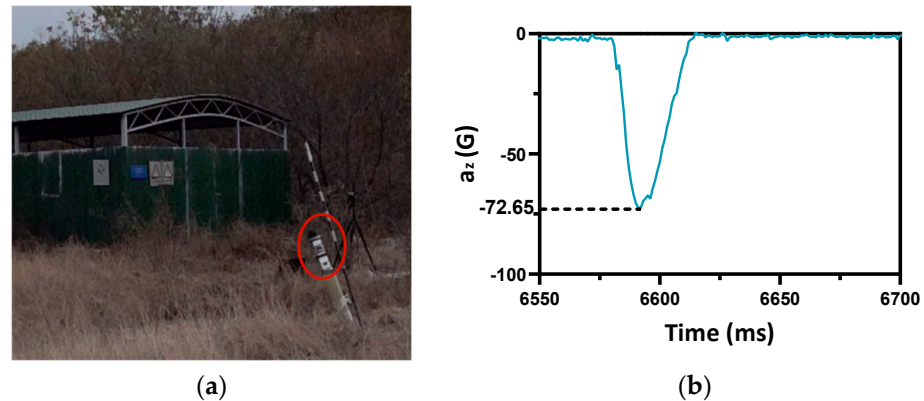

(**a**)   (**b**)

Figure 10. Plot of the simulated load barrel shot experiment. (**a**) Moment when the simulated load barrel shot out of the barrel. (**b**) Recorded values of z-direction acceleration data after the simulated load barrel launching.

5.2. Static Experiment

The parameters of the drone are incorporated into the simulation system, and the simulation software is Matlab 2022a. The purpose of the simulation is to verify the stability of the algorithm under large attitude and z-direction impacts, especially for the pitch direction. The Peregrine Falcon was commanded to track (roll, pitch) from (0, −20) to (0, 0), and the results are shown in Figure 11a. As shown in Figure 11b, the Peregrine Falcon can be stabilized quickly under a z-direction initial velocity of 10 m/s impact.
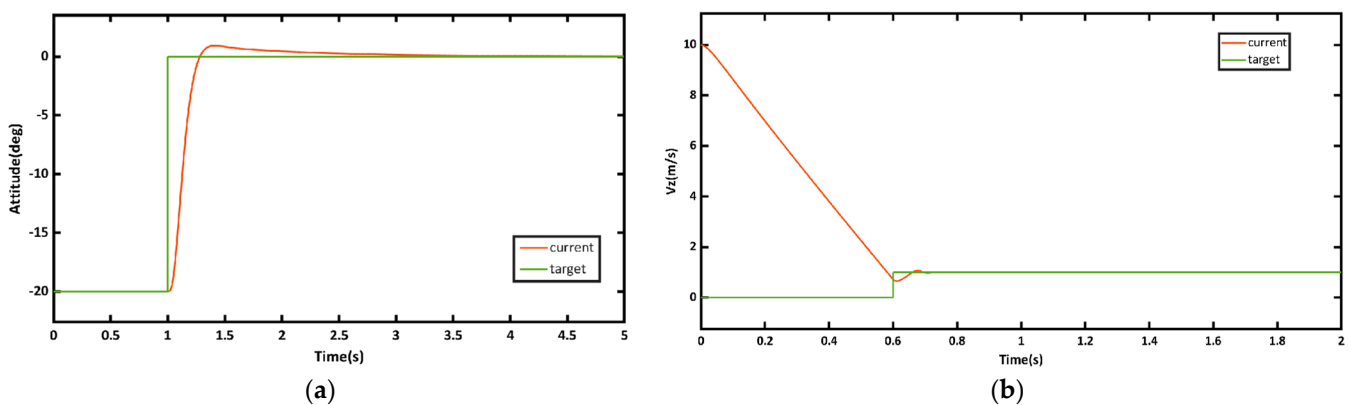

(**a**)   (**b**)

Figure 11. Simulation result. (**a**) Attitude tracking curve. (**b**) Climb rate tracking curve.

The static flying experiments were conducted using the above launch barrels placed at an angle of 70 degrees. The experimental data and images are shown in Figure 12. The whole task consists of several phases, including launching from the barrels (a), the spreading of the arms (b), the attitude control (c), and the control of the rate of climb (d). The data sampling frequency is 10 HZ. In stages a and b, the Peregrine Falcon attitude and altitude are not controlled, and only the barrel detection and autonomous arm extension

are performed. From the pitch angle data, the initial angle of the Peregrine Falcon before launch is 20°. Affected by the change in air pressure in the barrel during the launch, the altitude curve in stage a will have a negative value. Attitude control of the Peregrine Falcon starts in stage c, and climb rate control starts in stage d.

Figure 12. Static experiments on the barrel launching process. (**a**) The launch barrel phase; (**b**) the spread arm phase; (**c**) the attitude control phase; and (**d**) the climb rate control phase.

As shown by the attitude curves (Figure 13a,b), the Peregrine Falcon almost completes the convergence and stabilization of the pitch angle and roll angle at the 15th s. As shown in Figure 13c, the climb rate of the Peregrine Falcon nearly finishes convergence and stabilizes to 100 cm/s in the 15th s. As can be seen in the altitude curve (Figure 13d), the drone only controls the climb rate and the position after phase d but does not control the altitude. Since the climb rate has been maintained at 100 cm/s, the altitude direction will keep rising. In the 17th s, the controller switches the mode to LOITER mode, and at this point, the Peregrine Falcon starts to track the altitude direction.

Figure 14 shows the GPS trajectory of the Peregrine Falcon during the barrel launch test. Barrel shooting occurs from the start point. The blue curve shows the trajectory of the Peregrine Falcon in the launch mode. When the Peregrine Falcon reaches the altitude of 16.53 m, the attitude control and the climb rate control are completed and stabilized, and then the pilot switches to the LOITER mode by remote control (red curve) and finally controls it to land at the end point.

According to the performance test results, as shown in Figure 15a, the Peregrine Falcon can reach a maximum speed of 16.66 m/s. At the same time, the Peregrine Falcon is equipped with a 6 s lithium-polymer battery, with a full voltage of 25.1 V. As shown in Figure 15b, the voltage starts to change in the 64.3th s, which indicates that there is a load doing work, and at this time, it is believed that the drone propellers start to rotate. At the 712.8th s, the power is exhausted to 21.6 V when landing. The total time consumed is 648.5 s to meet the design expectation.
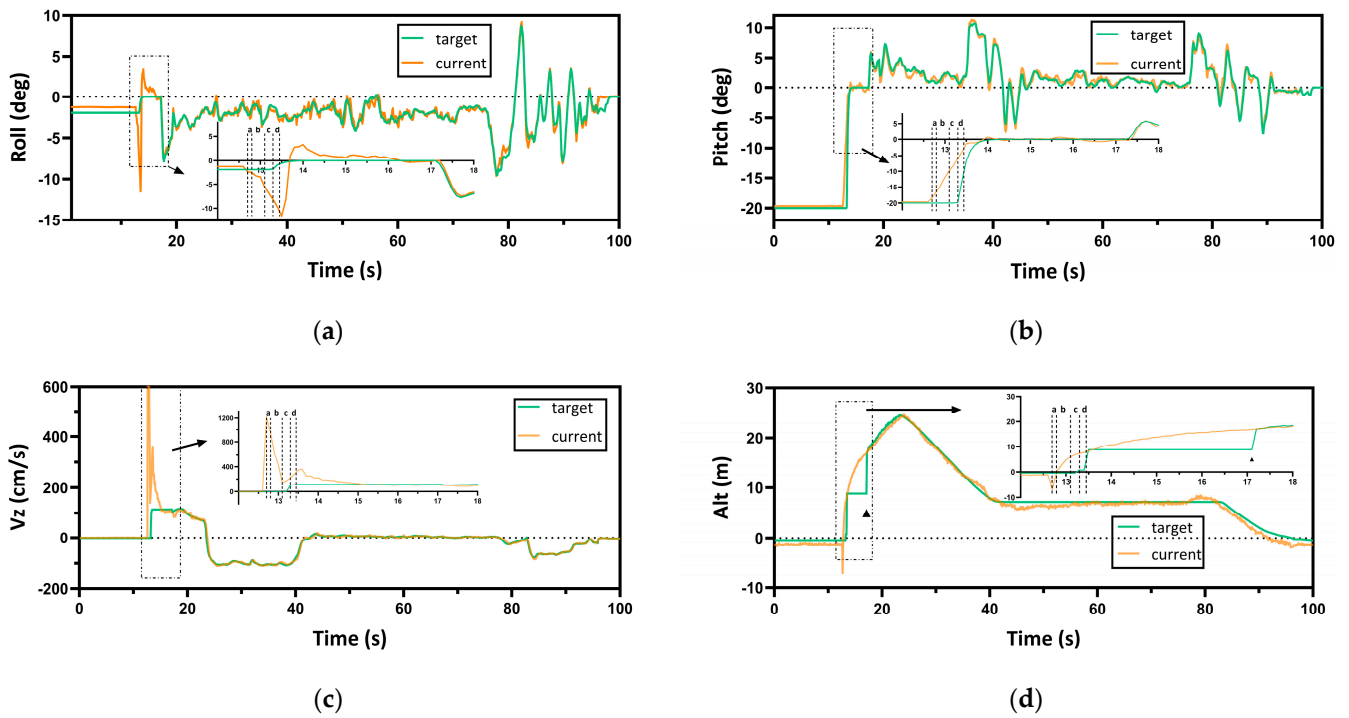
Figure 13. Static experimental results. (**a**) Roll angle tracking curve during launch; (**b**) pitch angle tracking curve during launch; (**c**) climb rate tracking curve during launch; and (**d**) altitude tracking curve during launch, where a, b, c, and d in the curves correspond to the stages presented in Figure 11.
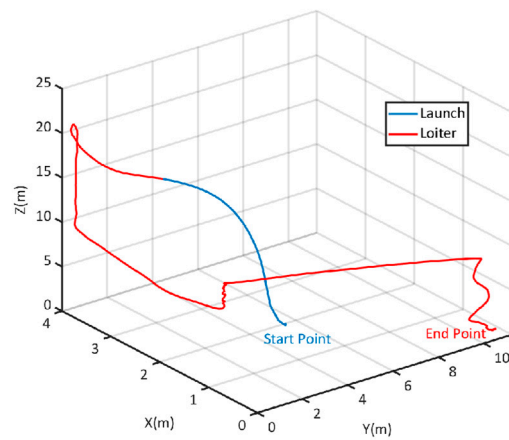

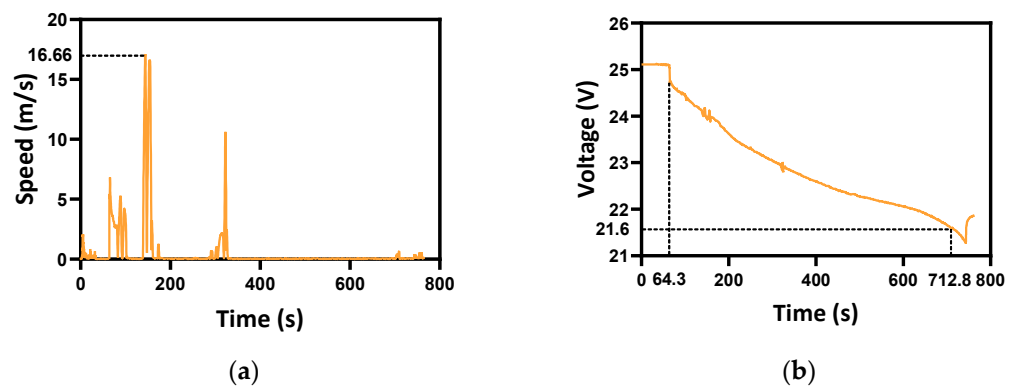**Figure 14.** The Peregrine Falcon trajectory in the static experiment.

Figure 15. Performance test. (**a**) Peregrine falcon speed curve and (**b**) voltage variation curve.

5.3. Dynamic Experiment

The launch barrel was first installed on an unmanned vehicle at an angle of 70 degrees, and the Peregrine Falcon was launched when the unmanned vehicle reached a speed of 11 km/h at a constant speed (Figure 16b). As can be seen in Figure 16c,d, the Peregrine Falcon was able to successfully complete the spreading arm action and achieve attitude and climb rate stabilization after launching.
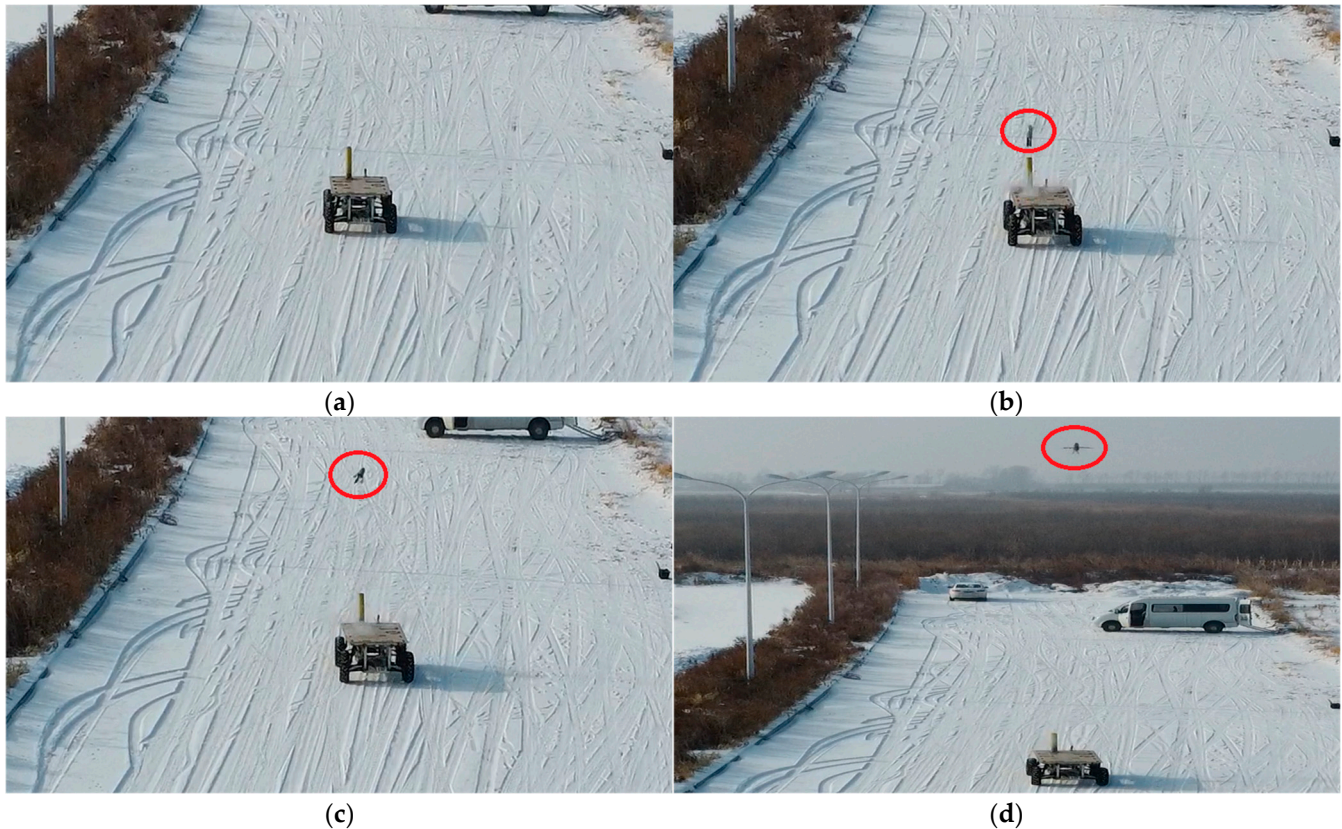

(**a**)

(**b**)

(**c**)

(**d**)

Figure 16. Dynamic experiment on the barrel launching process. (**a**) The cylinder standby phase; (**b**) the launch phase; (**c**) the arm spreading phase; and (**d**) the attitude stabilization and climb rate control phase.

Figure 17a shows that the unmanned vehicle starts at the 360th s and gradually accelerates to 3.05 m/s and then moves forward at a constant speed. The Peregrine Falcon is launched dynamically during the unmanned vehicle's uniform speed. At the moment of the barrel launch, the speed of the unmanned vehicle is 3.54 m/s. The unmanned vehicle starts to decelerate after the Peregrine Falcon comes out of the barrel. In Figure 17b,c, it can be seen that the Peregrine Falcon achieves complete stabilization within 1 s of the start of attitude control. In Figure 17d, the Peregrine Falcon basically achieves stabilization within 3 s of the start of climb rate control.
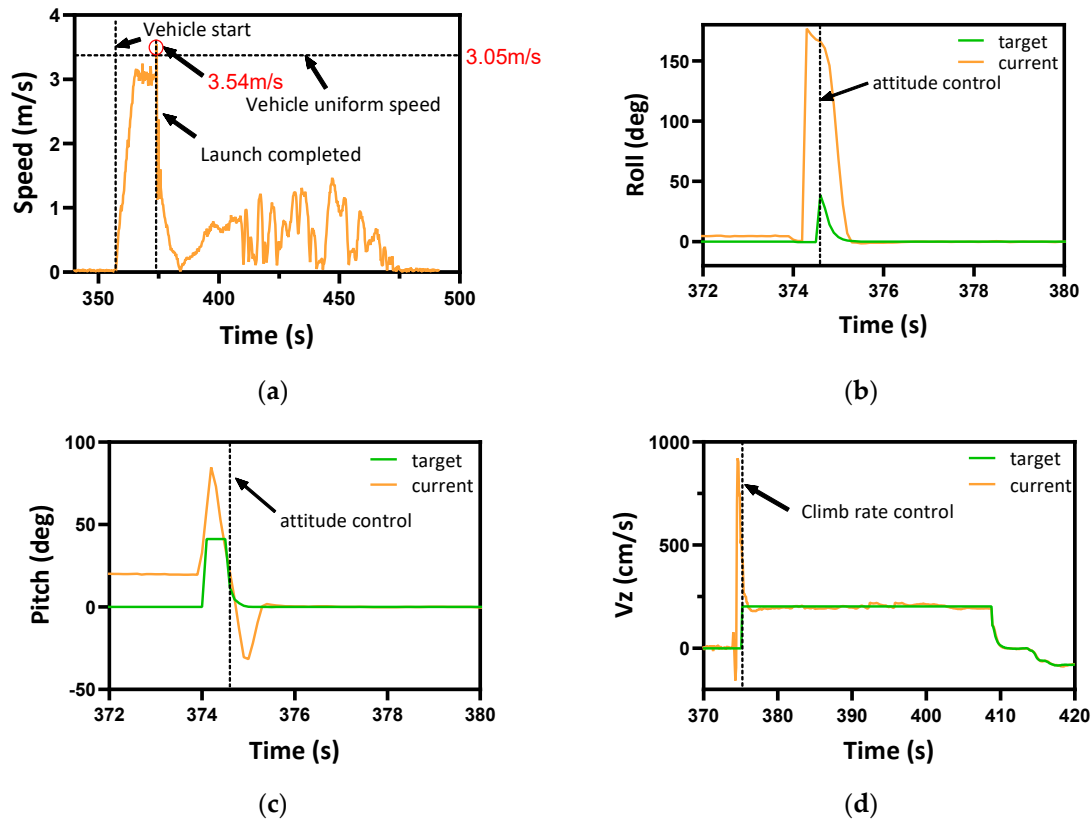
Figure 17. Dynamic experiment results. (**a**) Horizontal speed profile recorded from the start of the pre-launch; (**b**) roll angle tracking curve during launch; (**c**) pitch angle tracking curve during launch; and (**d**) climb rate tracking curve during launch.

6. Conclusions

The Peregrine Falcon is a drone designed for rapid mission execution, featuring a foldable fuselage that minimizes launch space requirements. By launching from a mobile vehicle, it significantly reduces the deployment time and mitigates the risk of injuries associated with rotating paddles during handheld takeoffs. In the future, this drone has the potential for applications in various industries, including urban anti-terrorism and firefighting reconnaissance.

At the same time, we shared every design step of this drone, including power matching, impact resistance design, electronic equipment selection, and algorithm design. The Peregrine Falcon has successfully demonstrated the capability of a barrel launch and autonomous control. It employs an attitude control algorithm that effectively addresses its stabilization and rapid convergence during large attitude changes in the air, and a climb rate control algorithm that quickly reduces impact-induced climb rate changes. It can withstand instantaneous accelerations up to 75 G, can carry launch 3-axis pod loads without damaging on-board components, and has tested control algorithms to launch to full 6-degree-of-freedom stabilization on a moving vehicle.

7. Future Work

To further validate the robustness of the system, the following future work will be carried out:

1. Conduct outdoor launching experiments in windward and crosswinds at wind speeds greater than 5 m/s. Verify the stability of the Peregrine Falcon after leaving the barrel under windy conditions.

2. Launch the Peregrine Falcon from a faster moving vehicle. Increase the speed of the unmanned vehicle to 30 km/h to verify the stability of the Peregrine Falcon after the barrel launch under fast-moving conditions.
3. Planned external improvements include a fuselage shell that boosts some of the lift to extend the time of the unpowered ascent phase of the barrel launch. This will help to adjust the subsequent barrel launch process.
4. The plan is to enable Peregrine Falcon to land on mobile vehicles by means of QR code identification.

Author Contributions: Conceptualization, G.W., L.N. and D.W. (Dong Wang 1); methodology G.W. and D.W. (Dong Wang 2); validation, G.W., D.W. (Dong Wang 2) and H.Z.; structure analysis, D.W. (Dong Wang 1); investigation, G.W. and H.Z.; resources, G.W.; data curation, H.Z.; writing—original draft preparation, G.W.; writing—review and editing, Y.B.; visualization, G.W.; project administration, X.P.; funding acquisition, Y.B. and L.N. All authors have read and agreed to the published version of the manuscript.

Data Availability Statement: The data presented in this study are available on request from the corresponding author. Original data can be obtained by contacting the corresponding author.

Conflicts of Interest: The authors declare no conflicts of interest.

References

1. Zheng, X. Throw Type Foldable Rotor UAV Design and Simulation Analysis. Master's Thesis, Shenyang Ligong University, Shenyang, China, 2023.
2. Gokbel, E.; Gullu, A.; Ersoy, S. Improvement of UAV: Design and implementation on launchability. *Aircr. Eng. Aerosp. Technol.* **2023**, *95*, 734–740. [CrossRef]
3. Huang, H.; Savkin, A.V. An Algorithm of Reactive Collision Free 3-D Deployment of Networked Unmanned Aerial Vehicles for Surveillance and Monitoring. *IEEE Trans. Ind. Inform.* **2020**, *16*, 132–140. [CrossRef]
4. Wolek, A.; Cheng, S.; Goswami, D.; Paley, D.A. Cooperative Mapping and Target Search Over an Unknown Occupancy Graph Using Mutual Information. *IEEE Robot. Autom. Lett.* **2020**, *5*, 1071–1078. [CrossRef]
5. Tuna, T.; Ovur, S.E.; Gokbel, E.; Kumbasar, T. Design and development of FOLLY: A self-foldable and self-deployable quadcopter. *Aerosp. Sci. Technol.* **2020**, *100*, 105807. [CrossRef]
6. Bucki, N.; Mueller, M.W. Design and control of a passively morphing quadcopter. In Proceedings of the 2019 International Conference on Robotics and Automation (ICRA), Montreal, QC, Canada, 20–24 May 2019; pp. 9116–9122.
7. Devlin, T.; Dickerhoff, R.; Durney, K.; Forrest, A.; Pansodtee, P.; Adabi, A.; Teodorescu, M. Elbowquad: Thrust vectoring quadcopter. In *2018 AIAA Information Systems-AIAA Infotech@ Aerospace*; Aerospace Research Central: Arlington, VA, USA, 2018; p. 0893.
8. Xu, J.; Hao, Y.; Wang, S. Flight control simulation and flight test of foldable rotor uav. *Proc. J. Phys. Conf. Ser.* **2022**, *2252*, 012052. [CrossRef]
9. Bai, Y.; Jin, Y.; Liu, C.; Zeng, Z.; Lian, L. Nezha-F: Design and analysis of a foldable and self-deployable HAUV. *IEEE Robot. Autom. Lett.* **2023**, *8*, 2309–2316. [CrossRef]
10. Lu, D.; Xiong, C.; Zhou, H.; Lyu, C.; Hu, R.; Yu, C.; Zeng, Z.; Lian, L. Design, fabrication, and characterization of a multimodal hybrid aerial underwater vehicle. *Ocean Eng.* **2021**, *219*, 108324. [CrossRef]
11. Yang, L.; Kaisong, W.; Wei, T.; Kecheng, Q.; Tao, Z.; Zhan, Y.; Jun, Z. Design and Implementation of Foldable Winged Amphibious UAV Based on Tilting Motor. *J. Mech. Eng.* **2024**, *60*, 272–286.
12. Yu, Y.; Yang, S.; Wang, M.; Li, C.; Li, Z. High performance full attitude control of a quadrotor on SO (3). In Proceedings of the 2015 IEEE International Conference on Robotics and Automation (ICRA), Seattle, WA, USA, 26–30 May 2015; pp. 1698–1703.
13. Zhang, L.; Gong, X.Y.; Zhou, M. Dynamic Simulation of a Motor-driven Mini-UAV's Hand-throwing Process. *Fire Control Command Control* **2015**, *40*, 152–155+160.
14. Guruge, P.; Kocer, B.B.; Kayacan, E. A novel automatic UAV launcher design by using bluetooth low energy integrated electromagnetic releasing system. In Proceedings of the 2015 IEEE Region 10 Humanitarian Technology Conference (R10-HTC), Cebu, Philippines, 9–14 December 2015; pp. 1–4.
15. Patterson, A.J.; Arena, A.S. A launch system design methodology for small unmanned aircraft applications. In Proceedings of the AIAA Atmospheric Flight Mechanics Conference, Kissimmee, FL, USA, 5–9 January 2015; p. 2858.

16. Zhang, X.; Mi, C.; Wu, X.; Che, F.; Zhang, H.; Luo, G. A Test, Launch and Control System for Ground Launched Loitering Munition. In Proceedings of the 2022 6th International Conference on Measurement Instrumentation and Electronics (ICMIE), Hangzhou, China, 17–19 December 2022; pp. 34–38.

17. Kessler, S.S. *Design and Manufacture of a High-G Unmanned Aerial Vehicle Structure*; Massachusetts Institute of Technology: Cambridge, MA, USA, 2000.

18. Yuan, X.; Jiang, D.; Zhou, Q.; Zheng, D.; Wang, L. Research on the Application of a Mortar Launched Unmanned Aerial Vehicle. *J. Ordnance Equip. Eng.* **2018**, *39*, 105–109.

19. Gnemmi, P.; Meder, K.; Rey, C. Aerodynamic performance of a gun launched micro air vehicle. *Int. J. Micro Air Veh.* **2012**, *4*, 251–272. [CrossRef]

20. Gnemmi, P.; Changey, S.; Meder, K.; Roussel, E.; Rey, C.; Steinbach, C.; Berner, C. Conception and manufacturing of a projectile-drone hybrid system. *IEEE/ASME Trans. Mechatron.* **2017**, *22*, 940–951. [CrossRef]

21. Pastor, D.; Izraelevitz, J.; Nadan, P.; Bouman, A.; Burdick, J.; Kennedy, B. Design of a ballistically-launched foldable multirotor. In Proceedings of the 2019 IEEE RSJ International Conference on Intelligent Robots and Systems (IROS), Macau, China, 3–8 November 2019; pp. 5212–5218.

22. Bouman, A.; Nadan, P.; Anderson, M.; Pastor, D.; Izraelevitz, J.; Burdick, J.; Kennedy, B. Design and autonomous stabilization of a ballistically-launched multirotor. In Proceedings of the 2020 IEEE International Conference on Robotics and Automation (ICRA), Paris, France, 31 May–31 August 2020; pp. 8511–8517.

23. Lopez-Sanchez, I.; Moreno-Valenzuela, J. PID control of quadrotor UAVs: A survey. *Annu. Rev. Control* **2023**, *56*, 100900. [CrossRef]

24. Wang, L.; Wang, J. Four-rotor UAV Special Ammunition Hovering-launch Mechanics Research. *J. Ballist* **2022**, *34*, 38–44.

25. Lian, S.; Meng, W.; Shao, K.; Zheng, J.; Zhu, S.; Li, H. Full attitude control of a quadrotor using fast nonsingular terminal sliding mode with angular velocity planning. *IEEE Trans. Ind. Electron.* **2022**, *70*, 3975–3984. [CrossRef]

26. Brescianini, D.; Hehn, M.; D'Andrea, R. *Nonlinear Quadrocopter Attitude Control: Technical Report*; ETH Zurich: Zurich, Swizterland, 2013.